



ARTICLE

## Research on Infrared Emissivity and Laser Reflectivity of $\text{Sn}_{1-x}\text{Er}_x\text{O}_2$ Micro/Nanofibers Based on First-Principles

Yuanjia Xia, Fang Zhao\*, Zhizun Li, Zhaogang Cheng and Jianwei Hu

Shijiazhuang Campus, Army Engineering University of PLA, Shijiazhuang, 050003, China

\*Corresponding Author: Fang Zhao. Email: zhaofang19821106@163.com

Received: 28 March 2022 Accepted: 06 May 2022

### ABSTRACT

$\text{Sn}_{1-x}\text{Er}_x\text{O}_2$  ( $x = 0\%$ ,  $8\%$ ,  $16\%$ ,  $24\%$ ) micro/nanofibers were prepared by electrospinning combined with heat treatment using erbium nitrate, stannous chloride and polyvinylpyrrolidone (PVP) as raw materials. The target products were characterized by thermogravimetric analyzer, X-ray diffractometer, fourier transform infrared spectrometer, scanning electron microscope, spectrophotometer and infrared emissivity tester, and the effects of  $\text{Er}^{3+}$  doping on its infrared and laser emissivity were studied. At the same time, the  $\text{Sn}_{1-x}\text{Er}_x\text{O}_2$  ( $x = 0\%$ ,  $16\%$ ) doping models were constructed based on the first principles of density functional theory, and the related optoelectronic properties such as their energy band structure, density of states, reflectivity and dielectric constant were analyzed, and further explained the mechanism of  $\text{Er}^{3+}$  doping on  $\text{SnO}_2$  infrared emissivity and laser absorption from the point of electronic structure. The results showed that after calcination at  $600^\circ\text{C}$ , single rutile type  $\text{SnO}_2$  was formed, and the crystal structure was not changed by doping  $\text{Er}^{3+}$ . The calcined products showed good fiber morphology, and the average fiber diameter was 402 nm. The infrared emissivity and resistivity of the samples both decreased first and then increased with the increase of  $\text{Er}^{3+}$  doping amount. When  $x = 16\%$ , the infrared emissivity of the sample was at least 0.71; and  $\text{Er}^{3+}$  doping can effectively reduce the reflectivity of  $\text{SnO}_2$  at  $1.06 \mu\text{m}$  and  $1.55 \mu\text{m}$ , when  $x = 16\%$ , its reflectivity at  $1.06 \mu\text{m}$  and  $1.55 \mu\text{m}$  are 50.5% and 40%, respectively, when  $x = 24\%$ , the reflectivity at  $1.06 \mu\text{m}$  and  $1.55 \mu\text{m}$  wavelengths are 47.3% and 42.1%, respectively. At the same time, the change of carrier concentration and electron transition before and after  $\text{Er}^{3+}$  doping were described by first-principle calculation, and the regulation mechanism of infrared emissivity and laser reflectivity was explained. This study provides a certain experimental and theoretical basis for the development of a single-type, light-weight and easily prepared infrared and laser compatible-stealth material.

### KEYWORDS

Micro/nano fibers;  $\text{Er}^{3+}$  doping;  $\text{SnO}_2$ ; laser and infrared compatible stealth material

## 1 Introduction

With the rapid development of military science and technology, all kinds of new intelligent detection equipment are emerging, which makes military targets face severe threats. Traditional single-band stealth materials are difficult to cope with diversified detection technologies, and multi spectrum compatible stealth materials are expected to meet the actual needs of various military targets in complex battlefield environment. Infrared and laser compatible stealth materials are one of the key points in the research of



multi spectrum compatible stealth materials [1–4]. At present, the common laser and infrared compatible stealth materials mainly include photonic crystals [5], metamaterials [6], doped oxide semiconductors [7], etc. Photonic crystals and metamaterials are difficult to prepare and complex to design [1]. However, the traditional composite coating stealth materials have problems such as thick thickness and high density [8], so it is of great significance to study a single-type, light-weight and easily prepared laser and infrared compatible stealth material.

SnO<sub>2</sub>, as a typical wide-gap N-type oxide semiconductor material, has stable physical and chemical properties, high visible light transmittance and low resistivity. It is a photoelectric material with great development potential [9,10] and has been widely used in sensors, electrode materials, catalytic materials and other fields [11–14]. At the same time, it also has a wide application prospect as a multi spectrum compatible stealth material. Qiao et al. [15] prepared the core-shell structure Fe<sub>3</sub>O<sub>4</sub>@SnO<sub>2</sub> nanochain, and found that it has a high reflection loss in the radar operating band and a high reflectivity in the infrared band. The color of the material shows selective absorption of visible light, which is considered as a promising radar/infrared/visible compatible stealth material. Zhang et al. [16] synthesized SnO<sub>2</sub>@ZnO nanostructures by two-step hydrothermal method, whose lowest reflection loss is -23.51 dB at 9.2 GHz and bandwidth is 3.5 GHz, and the average infrared emissivity in mid-infrared band and far-infrared band is about 0.65 and 0.89, respectively. Qin et al. [7] synthesized Al and Sb co-doped SnO<sub>2</sub> composite by coprecipitation method. The study found that when Al content was 20% and Sn/Sb ratio was 10:1, its infrared emissivity was 0.708 and reflectivity was 43.4%, showing the best infrared laser compatibility and stealth performance. Rare earth elements are characterized by high charge, large ionic radius and strong self-polarization ability [17], so rare earth doping is considered to be an effective method to improve the photoelectric properties of materials, and has broad application prospects in the field of stealth materials [18]. In the early stage, our research group used La<sup>3+</sup> and Sm<sup>3+</sup> doped SnO<sub>2</sub> [19] respectively to explore its infrared emissivity, and it was confirmed that rare earth doping can effectively reduce the infrared emissivity of SnO<sub>2</sub>. As a typical heavy rare earth ion, Er<sup>3+</sup> ion has more electrons in its 4f electron layer and is less affected by the surrounding crystal field, and the spectral transition similarity in different substrates is strong, which can effectively improve the doping the optoelectronic properties of the system [20]. Li et al. [21] prepared camouflage ErCrO<sub>3</sub> powder material by high temperature solid-phase method, and found that it has strong absorption at 1.06 μm and 1.55 μm, and when the material thickness is about 0.2 mm, its maximum absorption rate of 1.55 μm is more than 60%, which is expected to become a kind of laser and visible light compatible stealth material. Ren et al. [22] prepared earth-red ErFeO<sub>3</sub> powder by high-temperature solid-phase method, and found that when the calcination temperature was 1300°C, the absorptivity of the material sample with a thickness of about 0.2 mm at 1.55 μm reached 37.5%, showing good absorption effect for laser. Zhang et al. [23] prepared Er<sup>3+</sup>-doped Y<sub>2</sub>O<sub>3</sub> upconversion nano-powder materials by wet chemical method. The results show that with the increase of doping concentration, the spectral reflectance of the material around 1.06 μm decreases correspondingly, and the minimum value is close to 0.1, which shows good laser stealth performance. However, there is no research on the use of heavy rare earth ions Er-doped SnO<sub>2</sub> in the field of infrared and laser compatible stealth. Due to the advantages of large surface area, light weight and high porosity, micro-nanofibers have great potential application value in the field of compatible stealth materials [24,25], which is more in line with the current development trend of lightweight stealth materials. First-principles calculations are an important way to study the microscopic electronic interaction mechanism of materials. Starting from the electronic structure, further explaining the ion doping mechanism can provide a new idea for the development of infrared and laser stealth materials.

Therefore, in this study, Sn<sub>1-x</sub>Er<sub>x</sub>O<sub>2</sub> (x = 0%, 8%, 16%, 24%) micro/nano fibers were prepared by electrostatic spinning method, and their infrared emissivity and laser reflectivity were investigated. At the same time, the doping system models were constructed by first-principles calculation, and the regulation mechanism of Er<sup>3+</sup> doping on

their infrared emissivity and laser reflectivity was further analyzed from the perspective of electronic structure. This work provides a certain experimental and theoretical basis for the development of “thin, light-weight, wide-band and high-performance” new infrared and laser compatible stealth materials.

## 2 Experiment and Simulation

### 2.1 Sample Preparation

Using analytical pure  $\text{SnCl}_2 \cdot 2\text{H}_2\text{O}$  (Tianjin Shentai Chemical Reagent Co., Ltd., China) and analytical pure  $\text{Er}(\text{NO}_3)_3 \cdot 6\text{H}_2\text{O}$  (Shanghai McLean Biochemical Technology Co., Ltd., China) as raw materials, a proper amount of raw materials were weighed and mixed according to the stoichiometric ratio of  $\text{Sn}_{1-x}\text{Er}_x\text{O}_2$  ( $x = 0\%$ ,  $8\%$ ,  $16\%$ ,  $24\%$ ), and dissolved in a certain amount of deionized water to prepare the mixed solution. Analytical pure polyvinylpyrrolidone (PVP) (Tianjin Yongda Chemical Reagent Co., Ltd., China) and analytical pure N, N-dimethylformamide (DMF) (Tianjin Jindong Tianzheng Fine Chemical Reagent Factory, China) of the same mass as the mixed solution were weighed and mixed for 12 h to prepare the spinning precursor. The spinning precursor was transferred into a syringe with a stainless-steel needle (23 G) for electrostatic spinning. The spinning process parameters were as follows: The voltage was 20 kV, the needle receiving distance was 20 cm, the solution advancing rate was 0.1 mm/min, and the receiving rate was 140 r/min. The precursor  $\text{Sn}_{1-x}\text{Er}_x\text{O}_2/\text{PVP}$  micro/nano fibers were dried at  $100^\circ\text{C}$  for 12 h, then placed in an intelligent temperature control box resistance furnace, heated to  $600^\circ\text{C}$  at a rate of  $1^\circ\text{C}/\text{min}$ , calcined for 2 h, and then cooled to room temperature with the furnace.

### 2.2 Sample Characterization

Thermogravimetric analysis was performed on the samples by differential thermogravimetric analysis analyzer (SDT-Q600, TA, USA). The phase of the samples were analyzed by polycrystalline X-ray diffractometer (XD6, Purkinje, China). The infrared spectra of the samples were analyzed by fourier transform infrared spectrometer (380, Nicole, USA). The morphology of the products were characterized by field emission scanning electron microscope (SU-8010, HITACHI, Japan). The elemental composition of the product was analyzed by X-ray energy dispersive spectrometer (Genesis Apex2, EDAX, USA). The diffuse reflectivity of the products were characterized by spectrophotometer (UV-3600, SHIMADZU, Japan) and integrating sphere (ISR-603, SHIMADZU, Japan). The calcined products were evenly mixed with the epoxy resin at the volume ratio of 1:1, coated on the ceramic sheet with smooth surface (diameter: 50 mm, thickness: 1 mm) by screen printing method, dried at  $100^\circ\text{C}$  for 2 h, and cooled naturally to room temperature, digital four-probe tester (ST2258C, JG, China) and infrared emissivity tester (IR-2, Chengbo, China) were used to test their resistivity and infrared emissivity.

### 2.3 Simulation Parameter Setting

The CASTEP module in Material Studio software was adopted, the electronic correlation potential was selected as GGA-PBE functional, and the electronic pseudopotential was selected as ultra-soft pseudopotential. The geometry optimization and energy calculation of all supercell models were carried out in reciprocal space without considering spin polarization effect. The parameters were set as follows: the plane wave cutoff energy was 400 eV, the K grid point of the Brillouin zone was  $3 \times 3 \times 4$ , the unit electron energy was  $2 \times 10^{-5}$  eV/atom, and the self-consistent accuracy was  $2.0 \times 10^{-6}$  eV/atom, the interatomic interaction force was less than  $0.05 \text{ eV}/\text{\AA}$ , and the stress deviation was less than 0.1 GPa. The selected valence electron configurations were: Sn ( $5s^25p^2$ ), O ( $2s^22p^4$ ) and Er ( $5p^64f^{12}6s^2$ ).

## 3 Results and Analysis

### 3.1 Analysis of Thermal Decomposition Process

Fig. 1 shows the TGA-DSC curve of  $\text{SnCl}_2/\text{PVP}$  precursor polymer. As can be seen from Fig. 1, the thermal decomposition process of precursor polymer can be divided into three stages: The first stage is

from room temperature to 170°C, and the mass loss is about 9.9%. At the same time, in the DSC curve, a small endothermic peak appears at 80°C, which is due to the volatilization of free water adsorbed on the surface of the precursor polymer, crystal water and residual solvent in the raw material [26]. The second stage is 170°C–500°C, the TGA curve shows a large weight loss step with a weight loss rate of about 54.9%. Especially between 300°C–400°C, the polymer shows a severe mass loss. Meanwhile, in the DSC curve, exothermic peaks appear around 325°C and 435°C, which are mainly caused by the decomposition of PVP and inorganic salts, that is, the conversion of SnCl<sub>2</sub> to SnO<sub>2</sub> [27]. The third stage is 500°C and above, the TGA curve tends to be horizontal, and the DSC curve has no exothermic peak, indicating that the thermal decomposition of the polymer in the precursor fiber is completed, that is, SnCl<sub>2</sub> has been completely converted into SnO<sub>2</sub>. Therefore, in order to make the product fully crystallized, the calcination temperature of SnCl<sub>2</sub>/PVP precursor fiber was set to 600°C in this experiment.

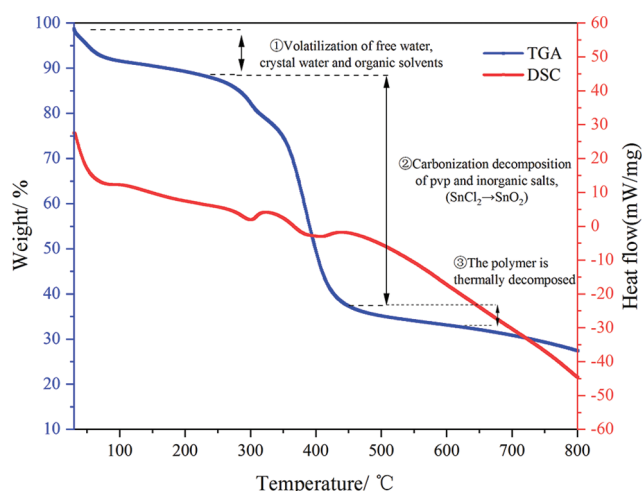


**Figure 1:** TGA-DSC curves of SnCl<sub>2</sub>/PVP precursor fibers

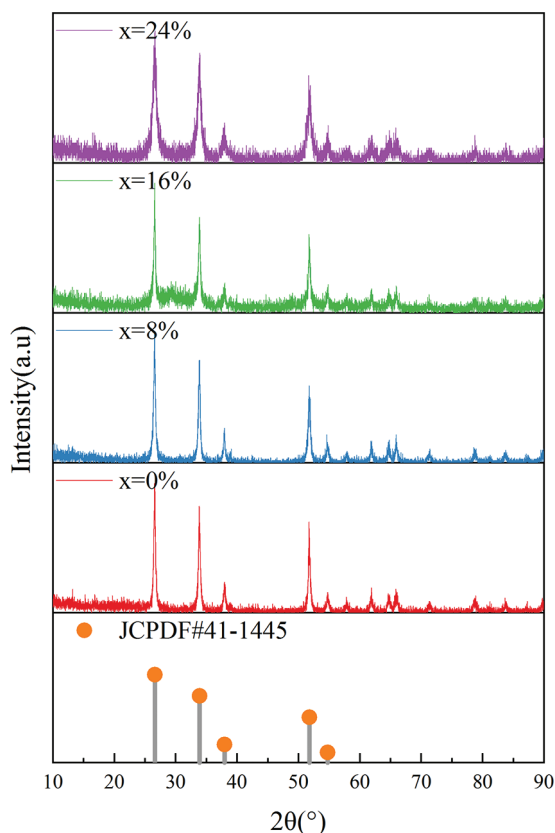
### 3.2 Phase Analysis

Fig. 2 shows the XRD spectra of Sn<sub>1-x</sub>Er<sub>x</sub>O<sub>2</sub> (x = 0%, 8%, 16%, 24%) micro/nano fibers calcined at 600°C for 2 h. It can be seen from Fig. 2 that the calcined products with different doping ratios all show obvious diffraction peaks on the crystal planes of (110), (101), (200), (211) and (220). The intensity of diffraction peak is consistent with that of JCPDF card No. 41-1445, indicating that the calcined products with different doping ratios are single tetragonal rutile SnO<sub>2</sub>. It can also be seen from Fig. 2 that with the increase of Er doping amount, the noise of the XRD pattern gradually increases, which may be due to the decrease of SnO<sub>2</sub> crystallinity with the increase of doping amount. At the same time, no diffraction peak of Er<sub>2</sub>O<sub>3</sub> is observed in the calcined products, indicating that Er<sup>3+</sup> has entered into the lattice of SnO<sub>2</sub>, and because the atomic radius of Er and Sn is close (Sn atomic radius is 0.158 nm, Er atomic radius is 0.176 nm, O atomic radius is 0.066 nm), Er atoms may enter into the SnO<sub>2</sub> lattice by replacing Sn atoms, which lays a foundation for the establishment of the simulation model later.

### 3.3 Infrared Spectral Analysis

In order to further characterize the structure of calcined products, FT-IR tests were performed on them respectively, as shown in Fig. 3. As can be seen from Fig. 3, absorption peaks of the products all appeared near 3434, 2374, 1637 and 619 cm<sup>-1</sup>. Among them, the absorption peaks near 3434 and 1637 cm<sup>-1</sup> are the stretching vibration of O-H bond and deformation vibration of adsorbed water molecule, which may be

caused by the water vapor adsorbed by the product in the air [28]. The absorption peak at  $2374\text{ cm}^{-1}$  is a characteristic peak of  $\text{CO}_2$ , which may be related to the stretching vibration of  $\text{CO}_2$  adsorbed on the surface of the sample [29]. The absorption peak near  $619\text{ cm}^{-1}$  is the characteristic absorption peak of  $\text{SnO}_2$  crystal, which can be assigned to the vibration band of Sn-O bond [30], which belongs to the  $E_u\text{TO}$  vibration mode [31]. Except for the above peaks, there are almost no other peaks, which further indicates that the products after calcination are all single tetragonal rutile  $\text{SnO}_2$ .



**Figure 2:** XRD patterns of calcined products with different doping ratios

### 3.4 Analysis of Microstructure and Material Composition

Fig. 4a is the SEM image of  $\text{SnCl}_2/\text{PVP}$  precursor micro/nano fibers. It can be seen from Fig. 4a that the precursor fibers have good fiber morphology, and the fibers are continuous and smooth, interleaving each other and presenting an irregular network structure. Fig. 4b is the SEM image of  $\text{Sn}_{0.84}\text{Er}_{0.16}\text{O}_2$  micro/nano fibers. It can be seen from Fig. 4b that after calcination at  $600^\circ\text{C}$ , the products still maintain good fibrous morphology, and the fibers surface are rough and composed of numerous fine  $\text{Sn}_{0.84}\text{Er}_{0.16}\text{O}_2$  micro/nano grains. Fig. 4c shows the diameter distribution of precursor fibers and  $\text{Sn}_{0.84}\text{Er}_{0.16}\text{O}_2$  fibers. It can be seen from Fig. 4c that after calcination at  $600^\circ\text{C}$ , the fiber diameter of the product decreases greatly, and its average diameter decreases from 785 to 402 nm. This is because in the calcination process, PVP and organic matter in the fibers are selectively burned out [32].

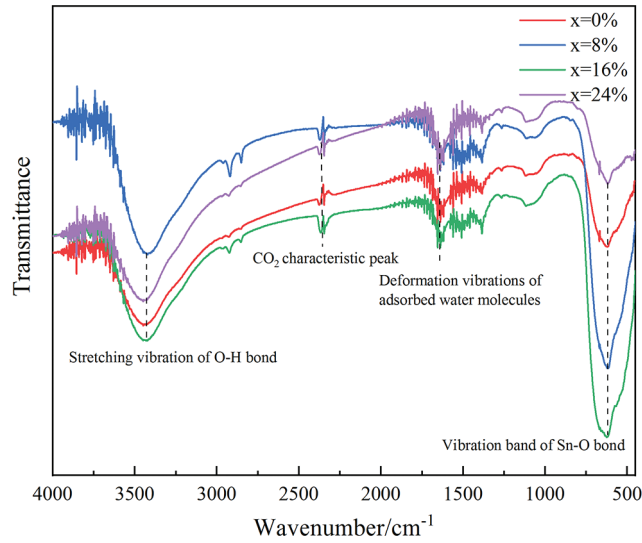


**Figure 3:** FT-IR spectra of calcined products with different doping ratios

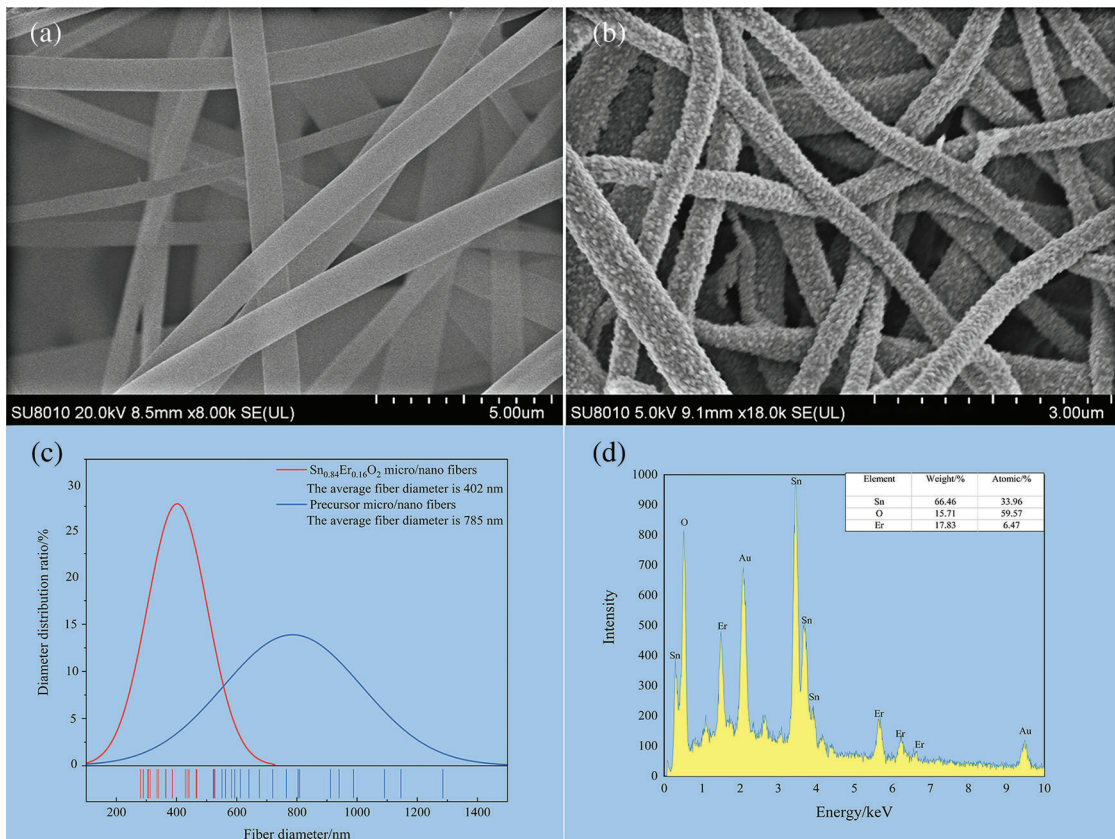


**Figure 4:** (a) SEM image of precursor fibers. (b) SEM image of  $\text{Sn}_{0.84}\text{Er}_{0.16}\text{O}_2$  fibers. (c) Diameter distribution of precursor fibers and  $\text{Sn}_{0.84}\text{Er}_{0.16}\text{O}_2$  fibers. (d) EDS spectra of  $\text{Sn}_{0.84}\text{Er}_{0.16}\text{O}_2$  fibers

In order to investigate the elemental composition of the heat treatment products, the energy spectrum analysis of  $\text{Sn}_{0.84}\text{Er}_{0.16}\text{O}_2$  micro/nano fibers was carried out. Fig. 4d shows EDS spectra of  $\text{Sn}_{0.84}\text{Er}_{0.16}\text{O}_2$  micro/nano fibers. As can be seen from Fig. 4d, except for Au treated by gold spraying, only Er, Sn and O elements exist in the sample, further indicating that after calcination at  $600^\circ\text{C}$ , PVP and other substances have been completely decomposed, which is consistent with XRD, FT-IR and TGA-DSC analysis. Moreover, the atomic ratio of Er to (Sn+Er) is about 16%, which is consistent with the expected doping ratio. Meanwhile, mapping was used to analyze the distribution of elements in the  $\text{Sn}_{0.84}\text{Er}_{0.16}\text{O}_2$  system of the product. The results are shown in Fig. 5. It can be seen from Fig. 5 that the distribution of elements in the fiber is uniform, indicating that  $\text{Sn}_{1-x}\text{Er}_x\text{O}_2$  micro/nano fibers with high purity and no impurities were prepared by electrostatic spinning method.

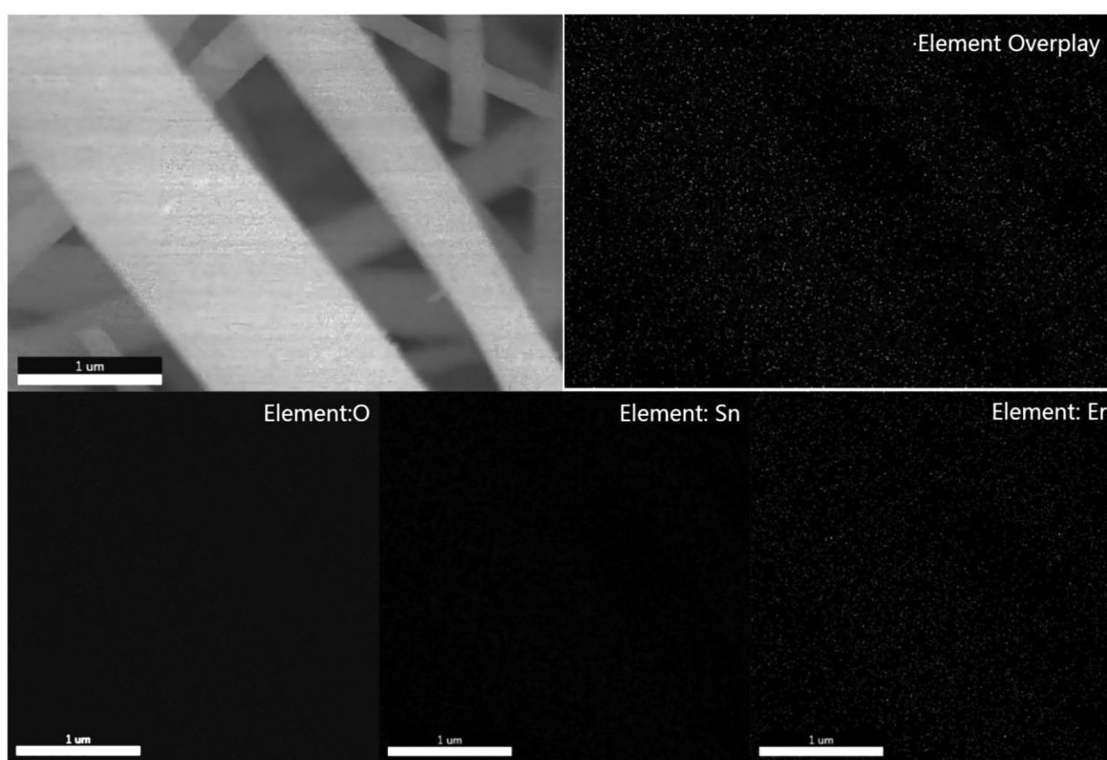


**Figure 5:** The distribution diagram of each element of  $\text{Sn}_{0.84}\text{Er}_{0.16}\text{O}_2$

### 3.5 Analysis of Resistivity and Infrared Emissivity

The operating bands of infrared detectors are generally  $3\text{--}5\ \mu\text{m}$  and  $8\text{--}14\ \mu\text{m}$ , of which  $8\text{--}14\ \mu\text{m}$  is the working band of thermal imaging system, and the threat of ground targets mainly comes from the infrared detection of this band. Fig. 6a shows the infrared emissivity and resistivity of  $\text{Sn}_{1-x}\text{Er}_x\text{O}_2$  micro/nano fibers. It can be seen from Fig. 6a that its infrared emissivity decreases first and then increases with the increase of doping ratio. When  $x = 16\%$ , its infrared emissivity is 0.71 at the lowest. In the working band of infrared light, since the photon energy of infrared light is less than the forbidden band width of the semiconductor, the absorption of infrared light by the semiconductor material mainly comes from the free

carriers in it. Therefore, by properly adjusting parameters such as the carrier concentration, collision frequency, and movement rate in the semiconductor material, the sample can have a lower infrared emissivity [33], which is related to its electrical properties and can be directly reflected by the resistivity. The resistivity of  $\text{Sn}_{1-x}\text{Er}_x\text{O}_2$  micro/nano fibers were tested, and the results are also shown in Fig. 6a. The resistivity and infrared emissivity show the same change trend, that is, with the increase of doping ratio, the resistivity of the sample decreases first and then increases. According to Hagen-Rubens law [34]:

$$E(\omega) \approx 2\sqrt{2\varepsilon_0\omega\rho} \quad (1)$$

where,  $E(\omega)$  is the infrared emissivity;  $\varepsilon_0$  is dielectric constant;  $\omega$  is the angular frequency of electromagnetic waves;  $\rho$  is the resistivity of the material. According to formula (1), the infrared emissivity of the material is positively correlated with the resistivity, that is, the lower the resistivity of the material, the stronger the electrical conductivity and the lower the infrared emissivity. The following two conditions are required for a material to have a certain conductivity: On the one hand, the carrier must be in a moving state inside the material, and its main expression form is hole and free electron.  $\text{SnO}_2$ , as a typical oxide semiconductor material, its carrier is mainly in the form of free electron in the lattice. It was found by XRD and FT-IR analysis that no new substances and new crystal forms were generated in the sample, indicating that  $\text{Er}^{3+}$  entered into the internal lattice of  $\text{SnO}_2$ . Due to the difference in price and ion radius between  $\text{Sn}^{4+}$  and  $\text{Er}^{3+}$ , a large number of oxygen vacancy defects and donor levels were generated when ion replacement occurred, providing a large number of free electrons for the acceptor levels. When excited, free electrons are more likely to transition from valence band to conduction band, which reduces the band gap width, reduces the resistivity and enhances the electrical performance [35]. However, as the doping ratio continues to increase, its resistivity increases slightly. This is because excessive doping may cause lattice distortion of  $\text{SnO}_2$ , resulting in interface enlargement and impurity ion scattering, thus changing the electron migration rate [36], resulting in a small increase in its resistivity. On the other hand, the interior of the material has a path for carriers to move. Micro/nanofibers have a special “three-dimensional network” morphology, which has the characteristics of large specific surface area and anisotropy, which can provide a convenient transport path for the transport of carriers and improve the electron transfer rate, so that it can effectively adjust the conductivity of the doped system [36–40], thereby further regulating the emissivity, as shown in Fig. 6b. Finally, it is shown in the previous article that the diameter of the prepared micro/nano fibers is about 400 nm, and the size of the micro-morphology also has a certain influence. The Mie scattering theory can be used for reference. It can be seen from Fig. 6c that when the fiber size is 400 nm, the incident light with wavelengths in the mid-far infrared region has entered the resonance region, which increases the scattering coefficient and reduces the infrared emissivity [41].

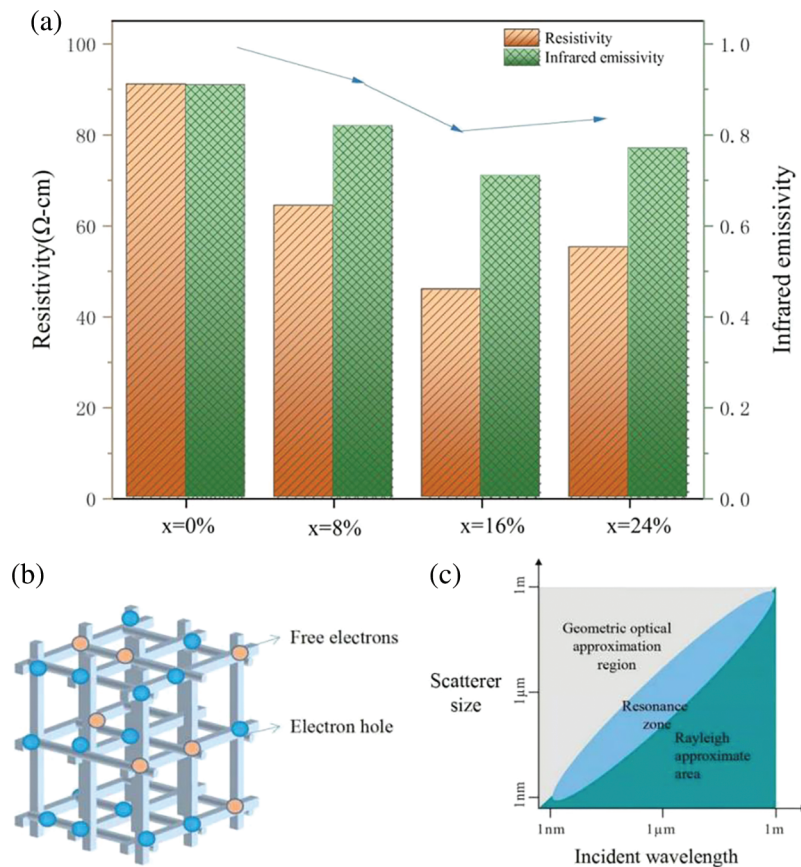


**Figure 6:** The diagram of infrared emissivity and resistivity variation and action mechanism of  $\text{Sn}_{1-x}\text{Er}_x\text{O}_2$  micro/nano fibers

### 3.6 Analysis of Laser Reflectivity

Fig. 7a shows the reflectivity of  $\text{Sn}_{1-x}\text{Er}_x\text{O}_2$  micro/nano fibers in the 500–2000 nm band. As can be seen from Fig. 7a,  $\text{Er}^{3+}$  doping can effectively reduce the reflectivity of the doping system at 1.06 and 1.55  $\mu\text{m}$  wavelengths, and  $\text{Sn}_{0.84}\text{Er}_{0.16}\text{O}_2$  and  $\text{Sn}_{0.76}\text{Er}_{0.24}\text{O}_2$  have small absorption peaks near 1.06 and 1.55  $\mu\text{m}$ . The reflectivity of  $\text{Sn}_{0.84}\text{Er}_{0.16}\text{O}_2$  system at 1.06 and 1.55  $\mu\text{m}$  is 50.5% and 40%, respectively, and that of  $\text{Sn}_{0.76}\text{Er}_{0.24}\text{O}_2$  system at 1.06 and 1.55  $\mu\text{m}$  is 47.3% and 42.1%, respectively.  $\text{Er}^{3+}$  doping reduces the reflectivity at 1.06 and 1.55  $\mu\text{m}$  for the following two reasons: On the one hand, semiconductor compounds are conductive materials with high concentration of free electron gas mode. According to the theory of semiconductor continuous spectrum, the propagation characteristics of light wave in visible infrared band are related to the plasma spectrum  $\omega_p$ , and the plasma frequency is also related to the carrier concentration in the doping system. After doping  $\text{Er}^{3+}$ , a new donor level ( $\text{Er}^{3+}$ ) is introduced into the doping system to provide more free electrons, which increases the carrier concentration and reduces the plasma frequency, strengthening the plasma effect [4]. And when the incident light frequency  $\omega > \omega_p$ , it has the characteristics of dielectric, with high transmittance and low reflectivity [42]. On the other hand, due to the excitation of  $\text{Er}^{3+}$  ions from the  $^4\text{I}_{15/2}$  energy level to the  $^4\text{I}_{11/2}$  energy level and the  $^4\text{I}_{13/2}$  energy level, the light waves around 1.06 and 1.55  $\mu\text{m}$  are absorbed [19]. Moreover, the number of electrons in the 4f electron layer of  $\text{Er}^{3+}$  ion is larger, which increases the probability of excited transition between f-f and f-d configuration. The schematic diagram of electron configuration and excited transition is shown in Fig. 7b. In addition, micro/nano fibers also play a certain role in the transmission of light

waves. Firstly, micro/nano fibers have small-scale effects, and their transmission and absorption rates of electromagnetic waves are greater than those of traditional micron powders [42]. Secondly, micro/nano fibers have large specific surface area and nonlinear characteristics, which promote charge transfer in the doped system and make them have efficient light absorption performance [37–38].

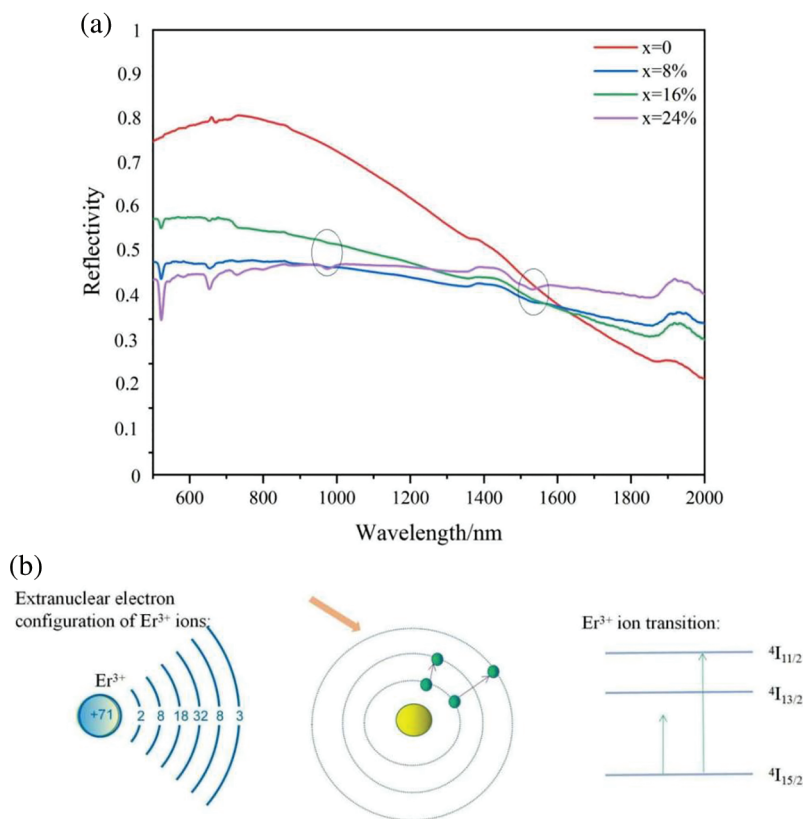


**Figure 7:** Reflectivity of  $\text{Sn}_{1-x}\text{Er}_x\text{O}_2$  micro-nanofibers in the 500–2000 nm band and schematic diagram of  $\text{Er}^{3+}$  ion transition

### 3.7 First-Principles Calculations

In the above analysis, it is found that the reduction of infrared emissivity and laser reflectivity by  $\text{Er}^{3+}$  doping is mainly due to the change of carrier concentration, and the change of carrier concentration is mainly because  $\text{Er}^{3+}$  doping increases the number of free electrons in the doping system, improves the probability of electron excitation, and thus improves its conductivity. Therefore, based on the first principle of density functional theory, this study compares and analyzes the energy band structure, state density, reflectivity, dielectric constant and other properties before and after  $\text{Er}^{3+}$  doping, and further expounds the mechanism of doping on infrared emissivity and laser reflectivity of doping system from the perspective of electronic structure.

In this study, a  $1 \times 2 \times 3$  supercell structure model was constructed, which contained 24 O atoms and 12 Sn atoms, as shown in Fig. 8a. In order to reduce the edge effect, the doping is realized by replacing the middle Sn atom with Er atoms, and the proportion of Er atoms is about 16%, which is consistent with the actual situation. The doping model is shown in Fig. 8b. Figs. 8c and 8d show the band structure of the intrinsic  $\text{SnO}_2$  and  $\text{Sn}_{0.84}\text{Er}_{0.16}\text{O}_2$  system, respectively, and it can be seen intuitively from Figs. 8c and 8d that after  $\text{Er}^{3+}$  doping, the density of the band structure is significantly increased, the band

structure is more gentle, and the electron localization is enhanced [43]. At the same time, the valence band width increases, impurity level increases, carrier concentration increases, the top of valence band passes through Fermi level, merger phenomenon occurs, and the doping system presents strong gold properties [44]. Moreover, the band gap width is reduced, making electrons easier to transition from valence band to conduction band and enhancing conductivity. Figs. 8e and 8f are the state densities of the intrinsic SnO<sub>2</sub> and Sn<sub>0.84</sub>Er<sub>0.16</sub>O<sub>2</sub> systems, respectively. It can be seen from Figs. 8e and 8f that the conduction band (0 to 23 eV) of the intrinsic SnO<sub>2</sub> system is mainly formed by the hybridization of 5s and 5p of Sn atoms. The upper valence band (0 to -8 eV) is formed by the joint hybridization of the 5s, 5p of the Sn atom and the 2p orbital of the O atom. Er<sup>3+</sup> doping causes the doped system to show a peak composed of 4f states of Er atoms near the Fermi level (-3 to 1 eV), which provides the energy of the conduction band and the upper valence band for the doped system, forming a large number of the impurity energy level, the degree of electron sharing is strengthened, the number of carriers is increased, and the electrical conductivity is improved [45]. From the analysis of the energy band structure and density of states, it can be seen that Er<sup>3+</sup> doping can effectively improve the electrical properties of the doped system, mainly due to the 4f state of the Er atom, which enhances the locality of the doped system near the Fermi level. The hybridization level increases, the forbidden band width decreases, and the carrier concentration increases. On the one hand, the increase of carrier concentration reduces the resistivity and thus the emissivity; On the other hand, the change of carrier concentration regulates the plasma wavelength, strengthens the plasma effect and reduces the laser reflectivity. The reflectivity of semiconductor materials is the macroscopic expression of the interband transition of electrons under the perturbation of the optical electromagnetic field [46]. The reflectivity of the intrinsic SnO<sub>2</sub> and Sn<sub>0.84</sub>Er<sub>0.16</sub>O<sub>2</sub> systems is shown in Fig. 8g. Compared with the intrinsic SnO<sub>2</sub> system, the Sn<sub>0.84</sub>Er<sub>0.16</sub>O<sub>2</sub> system has a lower emissivity in the band below 1.1 μm, and a higher reflectivity in the mid-far infrared band (3–5 μm), which makes the doped system have a lower emissivity in the infrared band. However, there are some errors between the simulation results and the above experimental tests. The reasons for this result may be as follows: On the one hand, the microscopic morphology and size of the material will have a certain influence on the photoelectric properties of the material [47,48]. In the previous paper, we also discussed the mechanism of the infrared emissivity and laser reflectivity of the fiber on the material. On the other hand, in the process of Er<sup>3+</sup> doping, all atomic substitutions cannot be realized, and lattice distortion may occur, which will affect the results [41,49]. The imaginary part of the dielectric constant represents the dipole formation energy, which can directly reflect the degree of electron excited transition. The larger the value, the higher the probability of transition [50]. The imaginary part of the dielectric constant of the intrinsic SnO<sub>2</sub> and Sn<sub>0.84</sub>Er<sub>0.16</sub>O<sub>2</sub> systems is shown in Fig. 8h, from which it can be seen: When the wavelength is larger than 600 nm, the imaginary part of dielectric constant of the intrinsic SnO<sub>2</sub> system decreases gradually and approaches 0, while the imaginary part of dielectric constant of the Sn<sub>0.84</sub>Er<sub>0.16</sub>O<sub>2</sub> system increases gradually and is much larger than that of the intrinsic SnO<sub>2</sub> system, indicating that the probability of electron excited transition increases greatly after Er<sup>3+</sup> doping. This is consistent with the previous analysis of the band structure and density of states, which together confirm the relevant theory of the experimental analysis.

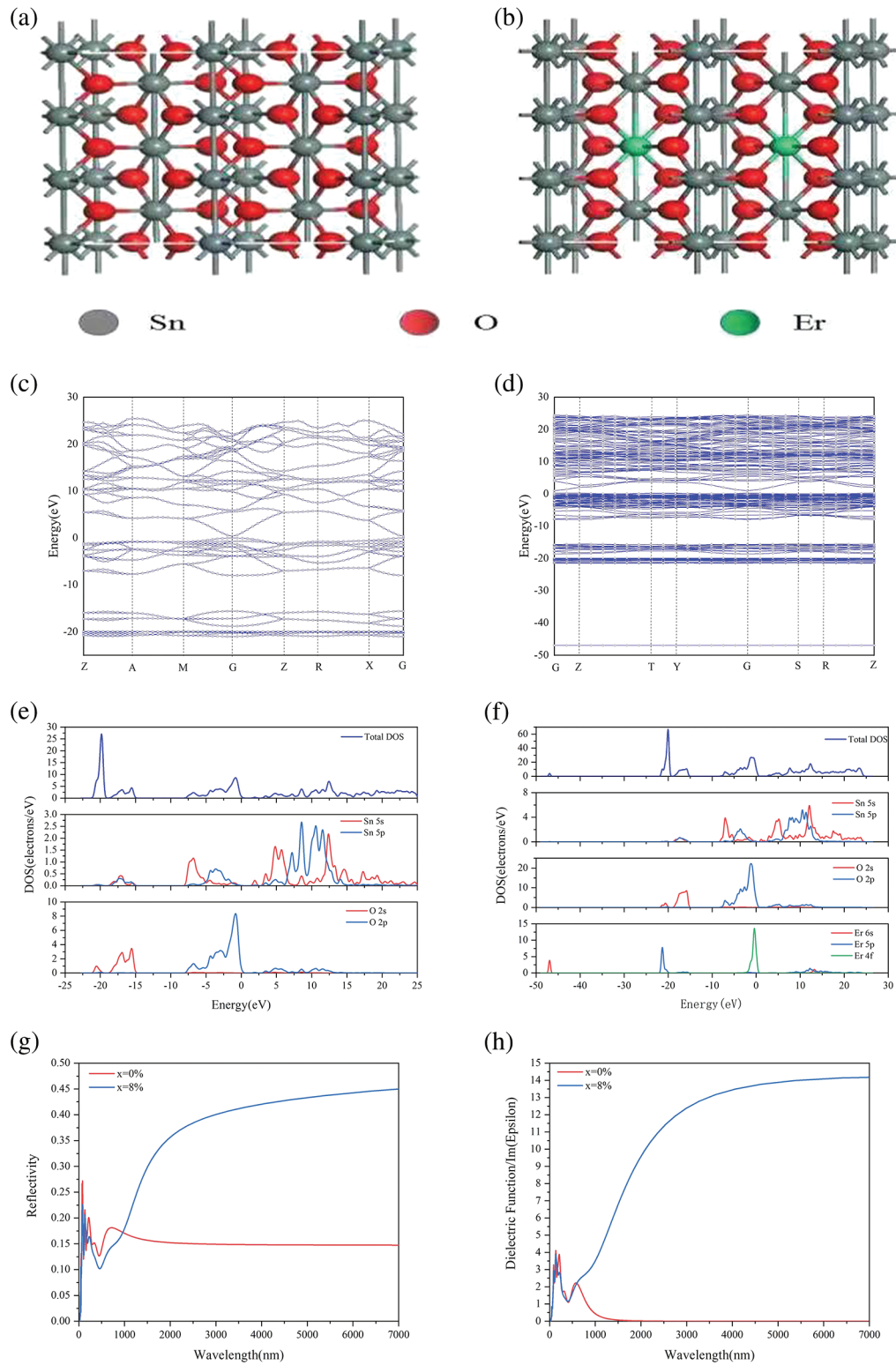


**Figure 8:** (a) Lattice model of SnO<sub>2</sub>. (b) Lattice model of Sn<sub>0.84</sub>Er<sub>0.16</sub>O<sub>2</sub>. (c) Band structure of SnO<sub>2</sub>. (d) Band structure of Sn<sub>0.84</sub>Er<sub>0.16</sub>O<sub>2</sub>. (e) DOS of SnO<sub>2</sub>. (f) DOS of Sn<sub>0.84</sub>Er<sub>0.16</sub>O<sub>2</sub>. (g) Reflectivity of SnO<sub>2</sub> & Sn<sub>0.84</sub>Er<sub>0.16</sub>O<sub>2</sub>. (h) Dielectric function (imaginary part) of SnO<sub>2</sub> & Sn<sub>0.84</sub>Er<sub>0.16</sub>O<sub>2</sub>

#### 4 Conclusion

- (1)  $\text{Sn}_{1-x}\text{Er}_x\text{O}_2$  ( $x = 0\%, 8\%, 16\%, 24\%$ ) micro/nano fibers were prepared by electrostatic spinning combined with heat treatment. The products all have a single rutile structure and show good fiber morphology.
- (2) With the increase of  $\text{Er}^{3+}$  doping concentration, infrared emission firstly decreases and then increases. When  $x = 16\%$ , it has the lowest infrared emissivity, which is 0.71. This is because  $\text{Er}^{3+}$  doping changes the carrier concentration of the doping system, and then changes its resistivity. At the same time,  $\text{Er}^{3+}$  doping can effectively reduce the laser reflectivity of the doped system, the reflectivity of the  $\text{Sn}_{0.84}\text{Er}_{0.16}\text{O}_2$  system at  $1.06 \mu\text{m}$  and  $1.55 \mu\text{m}$  is 50.5% and 40%, respectively. The reflectivity of  $\text{Sn}_{0.76}\text{Er}_{0.24}\text{O}_2$  system at  $1.06 \mu\text{m}$  and  $1.55 \mu\text{m}$  is 47.3% and 42.1%, respectively. On the one hand,  $\text{Er}^{3+}$  doping changes the plasma wavelength of the doping system and strengthens the plasma effect. On the other hand, it is due to the excitation of  $\text{Er}^{3+}$  ions from the  ${}^4\text{I}_{15/2}$  energy level to the  ${}^4\text{I}_{11/2}$  energy level and the  ${}^4\text{I}_{13/2}$  energy level to absorb the light waves around  $1.06 \mu\text{m}$  and  $1.55 \mu\text{m}$ .
- (3) The results of first-principles calculation of their electronic structure and optical properties show that: the reason for the improved infrared and laser compatible stealth performance of  $\text{Sn}_{1-x}\text{Er}_x\text{O}_2$  system is due to the 4f state of Er atom, the locality of the doped system near the Fermi level is enhanced, the hybridization level increases, and the degree of electron sharing is enhanced, the probability of electron excited transition is significantly improved, which effectively changes the infrared emissivity and laser reflectivity.

**Funding Statement:** This work was supported by the Key Research and Development Program of Hebei Province (No. 21351501D), A Provincial and Ministerial Scientific Research Project (LJ20212C031165) and Basic Frontier Science and Technology Innovation Project of Army Engineering University of PLA (KYSZJQZL2210).

**Conflicts of Interest:** The authors declare that they have no conflicts of interest to report regarding the present study.

#### References

1. Cheng, H. F., Huang, D. Q. (2014). Research progress in multi-spectrum compatible stealth material. *Journal of Aeronautical Materials*, 34(5), 93. DOI 10.11868/j.issn.1005-5053.2014.5.015.
2. Wang, X. K., Cheng, Z. G., Zhao, F., Wang, J. J., Li, Z. (2020). Electrospinning fabrication and infrared-radar compatible stealth properties of MWCNTs/ $\text{Zn}_{0.96}\text{Co}_{0.04}\text{O}$  composite nanofibers. *Rare Metal Materials and Engineering*, 49(12), 4262.
3. Wang, Y., Yu, M., Huang, C., Zheng, Q., Zhou, H. et al. (2021). Infrared emission characteristic and microwave loss property of aluminum doped zinc oxide nanoparticles. *Ceramics International*, 47(2), 2456–2462. DOI 10.1016/j.ceramint.2020.09.088.
4. Zhu, H., Li, Q., Tao, C., Hong, Y., Shen, W. et al. (2021). Multispectral camouflage for infrared, visible, lasers and microwave with radiative cooling. *Nature communications*, 12(1), 1–8. DOI 10.1038/s41467-021-22051-0.
5. Zhao, X., Zhao, Q., Wang, L. (2011). Laser and infrared compatible stealth from near to far infrared bands by doped photonic crystal. *Procedia Engineering*, 15(2), 1668–1672. DOI 10.1016/j.proeng.2011.08.311.
6. Kim, J., Han, K., Hahn, J. (2017). Selective dual-band metamaterial perfect absorber for infrared stealth technology. *Scientific Reports*, 7(1), 1–9. DOI 10.1038/s41598-017-06749-0.
7. Qin, Y., Zhang, M., Guan, Y., Huang, X. (2019). Laser absorption and infrared stealth properties of Al/ATO composites. *Ceramics International*, 45(11), 14312–14315. DOI 10.1016/j.ceramint.2019.04.144.
8. Zhang, J., Huang, X. G., Chen, J., Zhang, Q. T. (2011). Preparation and multiple-band stealth properties of  $\text{SmFeO}_3$ . *Journal of Functional Materials*, 2011, 1(42), 141.

9. Liang, J. N., Fu, C. L., Cai, W., Guo, Q., Zhang, C. Y. (2012). First-principle of transmissivity and conductivity of tin oxide doped with Indium. *Rare Metal Materials and Engineering*, 2012, 41(2), 197–199.
10. Yu, F., Wang, P. J., Zhang, C. W. (2010). First-principles study of optical and electronic properties of N-doped SnO<sub>2</sub>. *Acta Physica Sinica*, 2010, 59(10), 7288–7289.
11. Lin, Y., Wei, W., Li, Y., Li, F., Zhou, J. et al. (2015). Preparation of Pd nanoparticle-decorated hollow SnO<sub>2</sub> nanofibers and their enhanced formaldehyde sensing properties. *Journal of Alloys and Compounds*, 651, 690–698. DOI 10.1016/j.jallcom.2015.08.174.
12. Yi, J., Zhang, H., Zhang, Z., Chen, D. (2018). Hierarchical porous hollow SnO<sub>2</sub> nanofiber sensing electrode for high performance potentiometric H<sub>2</sub> sensor. *Sensors and Actuators B: Chemical*, 268, 456–464. DOI 10.1016/j.snb.2018.04.086.
13. Park, H., Song, T., Han, H., Devadoss, A., Yuh, J. et al. (2012). SnO<sub>2</sub> encapsulated TiO<sub>2</sub> hollow nanofibers as anode material for lithium ion batteries. *Electrochemistry communications*, 22, 81–84. DOI 10.1016/j.elecom.2012.05.034.
14. Ahn, K., Pham-Cong, D., Choi, H. S., Jeong, S., Cho, J. H. (2016). Bandgap-designed TiO<sub>2</sub>/SnO<sub>2</sub> hollow hierarchical nanofibers: Synthesis, properties, and their photocatalytic mechanism. *Current Applied Physics*, 16(3), 251–260. DOI 10.1016/j.cap.2015.12.006.
15. Qiao, M., Tian, Y., Li, J., He, X., Lei, X. et al. (2022). Core-shell Fe<sub>3</sub>O<sub>4</sub>@SnO<sub>2</sub> nanochains toward the application of radar-infrared-visible compatible stealth. *Journal of Colloid and Interface Science*, 609(11), 330–340. DOI 10.1016/j.jcis.2021.12.012.
16. Zhang, Z., Xu, M., Ruan, X., Yan, J., Yun, J. et al. (2017). Enhanced radar and infrared compatible stealth properties in hierarchical SnO<sub>2</sub>@ZnO nanostructures. *Ceramics International*, 43(3), 3443–3447. DOI 10.1016/j.ceramint.2016.11.034.
17. Jiang, B., Hu, S., Wang, M., Ouyang, X., Gong, Z. (2011). Synthesis and electrochemical performance of La-doped Li<sub>3</sub>V<sub>2-x</sub>La<sub>x</sub>(PO<sub>4</sub>)<sub>3</sub> cathode materials for lithium batteries. *Rare Metals*, 30(2), 115–119. DOI 10.1007/s12598-011-0208-6.
18. Wei, W., Liu, X., Lu, W., Zhang, H., He, J. (2019). Light-weight gadolinium hydroxide@polypyrrole rare-earth nanocomposites with tunable and broadband electromagnetic wave absorption. *ACS Applied Materials & Interfaces*, 11(13), 12752–12760. DOI 10.1021/acsami.8b21516.
19. Wang, X. K., Zhao, F., Tang, X. J., Duan, R. X., Wang, J. J. (2019). Electrospinning preparation and infrared-emissivity properties of La<sup>3+</sup>-doped SnO<sub>2</sub> hollow nanofiber. *Journal of Ceramics*, 40(3), 393–397. DOI 10.13957/j.cnki.txcb.2019.03.021.
20. Gnatenko, Y. P., Furyer, M. S., Bukivskii, A. P., Tarakhana, L. M., Gamernyk, R. V. (2015). Photoluminescence and photoelectric properties of CdTe crystals doped with Er atoms. *Journal of Luminescence*, 160, 258–261. DOI 10.1016/j.jlumin.2014.12.029.
21. Li, X. Y., Niu, C. H., Ren, X. W. (2016). Preparation method and laser camouflage performance of ErCrO<sub>3</sub>. *Laser Journal*, 37(3), 16–19. DOI 10.14016/j.cnki.jgzz.2016.03.016.
22. Ren, X. W., Lv, Y., Niu, C. H., Li, X. Y. (2016). Research on the preparation method and stealth performance of ErFeO<sub>3</sub>. *Laser & Infrared*, 49(9), 1148–1151. DOI 10.3969/j.issn.1001-5078.2016.09.025.
23. Zhang, S. Q., Shi, Y. L., Lu, Y. L. (2009). Analysis of the spectral properties of Er<sup>3+</sup>: Y<sub>2</sub>O<sub>3</sub> upconversion materials. *Acta Physica Sinica*, 58(4), 2768–2771.
24. Liu, X. F., Lai, Y. K., Huang, J. Y., Al-Deyab, S. S., Zhuang, K. Q. (2015). Hierarchical SiO<sub>2</sub>@Bi<sub>2</sub>O<sub>3</sub> core/shell electrospun fibers for infrared stealth camouflage. *Journal of Materials Chemistry C*, 3(2), 345–351. DOI 10.1039/C4TC01873G.
25. Fang, K. Y., Zhao, Y. C., Fang, F. (2021). Infrared stealth nanofibrous composite with thermal stability and mechanical flexibility. *Journal of Alloys and Compounds*, 855(6), 157418. DOI 10.1016/j.jallcom.2020.157418.
26. Song, Y., Zhao, F., Li, Z., Cheng, Z., Huang, H. et al. (2021). Electrospinning preparation and anti-infrared radiation performance of silica/titanium dioxide composite nanofiber membrane. *RSC Advances*, 11(39), 23901–23907. DOI 10.1039/D1RA03917B.

27. Tang, W., Wang, J., Qiao, Q., Liu, Z., Li, X. (2015). Mechanism for acetone sensing property of Pd-loaded SnO<sub>2</sub> nanofibers prepared by electrospinning: Fermi-level effects. *Journal of Materials Science*, 50(6), 2605–2615. DOI 10.1007/s10853-015-8836-0.
28. Yan, J., Cui, H. P., You, Y. C., Zhou, J. J. (2007). Effect of inorganic anion doping on the photocatalytic property of TiO<sub>2</sub> film. *Rare Metal Materials and Engineering*, 36(S1), 873–875.
29. Wagner, R. S., Ellis, W. C. (1964). Vapor-liquid-solid mechanism of single crystal growth. *Applied Physics Letters*, 4(5), 89–90. DOI 10.1063/1.1753975.
30. Wu, Y., Yang, P. (2001). Direct observation of vapor-liquid-solid nanowire growth. *Journal of the American Chemical Society*, 123(13), 3165–3166. DOI 10.1021/ja0059084.
31. Yang, P., Lieber, C. M. (1996). Nanorod-superconductor composites: A pathway to materials with high critical current densities. *Science*, 273(5283), 1836–1840. DOI 10.1126/science.273.5283.1836.
32. Pan, W., Ma, Z., Liu, J., Liu, Q., Wang, J. (2011). Effect of heating rate on morphology and structure of CoFe<sub>2</sub>O<sub>4</sub> nanofibers. *Materials Letters*, 65(21–22), 3269–3271. DOI 10.1016/j.matlet.2011.06.102.
33. Ma, G. L., Cao, Q. X., Huang, Y. X. (2003). Materials of infrared and radar multi-functional camouflage-doped semiconductor oxide. *Infrared Technology*, 25(4), 77–80.
34. Oguchi, H., Heilweil, E. J., Josell, D., Bendersky, L. A. (2009). Infrared emission imaging as a tool for characterization of hydrogen storage materials. *Journal of Alloys and Compounds*, 477(1–2), 8–15. DOI 10.1016/j.jallcom.2008.10.053.
35. Mei, S. B., Ning, W., Wang, Q. W., Jiang, S. H. (2009). Effects of La<sub>2</sub>O<sub>3</sub> doping on microstructure and resistivity of SnO<sub>2</sub>-based ceramics. *Journal of Synthetic Crystals*, 38, 943–947. DOI 10.16553/j.cnki.issn1000-985x.2009.04.015.
36. Tyuliev, G., Angelov, S. (1988). The nature of excess oxygen in Co<sub>3</sub>O<sub>4+ε</sub>. *Applied Surface Science*, 32(4), 381–391. DOI 10.1016/0169-4332(88)90089-X.
37. Ramakrishna, S., Fujihara, K., Teo, W. E., Yong, T., Ma, Z. et al. (2006). Electrospun nanofibers: Solving global issues. *Materials Today*, 9(3), 40–50. DOI 10.1016/S1369-7021(06)71389-X.
38. Kumar, P. S., Sundaramurthy, J., Sundarajan, S., Badu, V. J., Singh, G. et al. (2014). Hierarchical electrospun nanofibers for energy harvesting, production and environmental remediation. *Energy & Environmental Science*, 7(10), 3192–3222. DOI 10.1039/C4EE00612G.
39. Camposo, A., Persano, L., Pisignano, D. (2013). Light-emitting electrospun nanofibers for nanophotonics and optoelectronics. *Macromolecular Materials and Engineering*, 298(5), 487–503. DOI 10.1002/mame.201200277.
40. Lin, W. X., Liu, J. J. (2007). Laser and infrared stealth compatible materials-doped semiconductor. *Science Information*, (11), 50.
41. Tian, J. X. (2014). *Preparation and infrared emissivity of SnO<sub>2</sub> nanowires clusters (Ph.D. Thesis)*. Northwest University, China.
42. Zhang, Y. L., Li, P., Shi, L. (2018), *Stealth materials*, pp. 203–208. China: Chemical Industry Press.
43. Liang, Y. T., Wang, J. Q., Zhu, Y. C., Sun, S. Q., Zhang, Z. (2021). First principles study on the electrical conductivity of Sb and La co-doped SnO<sub>2</sub>. *Journal of Functional Materials*, 52(1), 1115–1119. DOI 10.3969/j.issn.1001-9731.2021.01.016.
44. Yu, S. M., Wang, J. J., Chen, L., Liu, Z. (2020). Electrical conductivity of Ce-Nd co-doped SnO<sub>2</sub> based on the first-principle. *Chinese Journal of Rare Metals*, 44(11), 1177–1183. DOI 10.13373/j.cnki.cjrm.xy19040015.
45. Sun, S. Q., Wang, J. J., Zhu, Y. C., Zhang, G. Z., Bao, Z. Z. (2020). First principle analysis of the conductivity of La-W co-doped SnO<sub>2</sub>. *Materials Reports*, 34, 48–52.
46. He, X., Wu, L. L., Li, C. X., Hao, X., Du, Z. (2020). First-principles investigation on electronic structure and optical properties of CdSe<sub>x</sub>S<sub>1-x</sub>. *Chinese Journal of Luminescence*, 41(2), 188–193. DOI 10.3788/fgxb20204102.0188.
47. Wang, F., Cheng, L., Mei, H., Zhang, Q., Zhang, L. (2014). Effect of surface microstructures on the infrared emissivity of graphite. *International Journal of Thermophysics*, 35(1), 62–75. DOI 10.1007/s10765-013-1533-9.

48. Botiz, I., Stingelin, N. (2014). Influence of molecular conformations and microstructure on the optoelectronic properties of conjugated polymers. *Materials*, 7(3), 2273–2300. DOI 10.3390/ma7032273.
49. Qu, S. Y. (2012). *Research on theories and experiments of infrared stealthy ZnO material with low-emissivity (Master Thesis)*. Xidian University, China.
50. Zhang, L. L., Xia, T., Liu, G. A., Lei, F. C., Zhao, X. C. et al. (2019). Electronic and optical properties of N-Pr co-doped anatase TiO<sub>2</sub> from first-principles. *Acta Physica Sinica*, 68(1), 17401. DOI 10.7498/aps.68.20181531.